Influence of directional wave spreading on a WEC device

E. Faraggiana, J. Chapman and I. Masters

Abstract— **Wave Energy Converter (WEC) performance is generally sensitive to the wave direction. So, it is important to include the effect of multi-directional waves in numerical modelling. A realistic representation of ocean waves should account for wave height and directional spreading parameters specific to the WEC deployment location. A high quality generalised directional distribution is dependent on the wave direction and frequency. Here we compare the power produced, the wave field, and the motion of the WaveSub device [1] for different frequency-directional distribution cases. Directional spreading has been modelled using different model distributions such as the uniform cosine fourth [2], Mitsuyasu [3], Hasselman [4] and Donelan-Banner [5], [6]. The hydrodynamic coefficients are computed for all wave directions using Nemoh [7]. Then, the WEC-Sim code [8] has been extended to add the capability to simulate different user selected frequency-directional spreading. The excitation force applied to each hydrodynamic body is updated to account for the effect of the directional spectrum. Results show that power produced is generally 10-20% lower than a single direction case. The motion of the device demonstrates the introduction of sway, roll, and yaw for the directional spreading simulations while the resultant wavefield is more uniform compared to the non-directional case. Computational time is significantly lower than comparable CFD approaches [9], [10] and this makes this method particularly effective.**

Manuscript received 22 October 2021; revised 5 August, accepted 6 September; published 30 September 2022.

Emilio Faraggiana is with the Marine Offshore Renewable Energy Lab at Polytechnic University of Turin, Corso Castelfidardo, 39, 10129, Turin, Italy (e-mail: emilio.faraggiana@polito.it).

John Chapman is with Marine Power Systems Ltd, The Warehouse Building Urban Village, Swansea SA1 2AQ, United Kingdom (e-mail: john.chapman@marinepowersystems.co.uk).

Ian Masters is with Energy and Environment Research Group, Zienkiewicz Centre for Computational Engineering, College of Engineering, Swansea University, United Kingdom (e-mail: i.masters@swansea.ac.uk).

Digital Object Identifier https://doi.org/10.36688/imej.5.227-242

Keywords— **Renewable Energy; wave energy; directional spreading.**

I. INTRODUCTION

In the search for a low-carbon future, devices that extract useful energy from their surroundings are a key part of the solution. Globally, ocean waves have a significant potential, and efforts to design wave energy converters (WECs) require accurate numerical models of the physics of the device interaction with the waves. Hybrid wind-wave devices have been also investigated in recent years as well as flexible body systems [11], [12]. The effect of wave directionality is an important factor to be investigated in the design and this is the subject of the present work. While the swell component of the wave can be adequately approximated with a unidirectional model, the wind-wave spectrum has a wave directional spread along the wind direction [13] that could have some influence on the performance of the device.

Directional spreading has been estimated from the free surface elevation at a single point in space with the assumption of a uniform Gaussian directional distribution independent from the wave frequency [14]. This is made by predicting the second order bound waves that are a function of the angle between the propagating waves. A more complex two-dimensional wave spectrum model has been developed in different studies [3]–[6]. Experimental data that included directional information were obtained in two studies, firstly, using a buoy capable of recording multiple forms of information (wave elevation, pitch and roll of the buoy) [4] or secondly, multiple wave gauges [5]. Measurements are clearly specific to the location of study. The JONSWAP site was used for [4] while [3] considered 5 typical datasets from the coast of Japan. In both cases the directional spectrum was described as a parametric model such as the $\cos^{2s}\frac{\theta}{2}$ where θ is the wave direction relative to the main direction but they used a different spreading function s because of the different location. Finally, [5] used measurements of the western end of lake Ontario and a different parametric model was obtained [5], [6].

The experimental study of [15] considered the Langlee device (a semi-submerged oscillating wave surge converter) and found a performance drop between 10-30% due to the directional spreading effect. An optimal

design of a vertical cylinder point absorber free to move in surge, heave and pitch is investigated for multi-directional waves in [2]. The power produced was demonstrated to be similar between the uni-directional spectrum and the directional one because of the symmetry of the device.

The directional distribution is found to influence the performance of a 6 degrees of freedom motion point absorber in [16] because sway, roll and yaw degrees of freedom are also excited. This paper used a nonlinear time-domain model with hydrodynamic coefficients from a Boundary Element Method (BEM) code, a nonlinear calculation of the Froude-Krylov force, and a Finite Element Method (FEM) to model the mooring lines.

A time-domain model of a point absorber influenced by the directional spread [17] was created in WEC-Sim [18], extending the software with the option of a directional spread that has since been included in the WEC-Sim release. However, this work was limited to modelling a uniform frequency-directional spread dependent only on the wave direction. Consequently, this paper aims to model the WaveSub device for a generic directional spread dependent on both the wave direction and frequency. The effect of the directional spread is evaluated by considering different available frequency-directional distributions from the literature [3]–[6] and comparing the response of the device in terms of power, motion, and wavefield generated. Each distribution case is optimised for the power take-off (PTO) parameters for a fairer comparison. The WaveSub device is a point absorber WEC under development by Marine Power Systems Ltd [1]. A spherical shaped float has been chosen to minimize the influence of the wave directional spreading. A description of its working principle can be found in [19]–[21]. The orbital motion of the float is converted into electricity thanks to the PTO lines that connect the float with the reactor. The PTO lines include 4 PTO lines in the corners (spring/damping PTO) and one in the centre (spring only). The central PTO line was designed to reduce the tension on the PTO corner lines due to the float buoyancy loading. The main reactor is a buoyant body in which is placed the PTO system. A taut mooring gives the required stability for a reliable and steady reactor base. Fig. 1 shows a multifloat configuration of the WaveSub device during the experimental campaign in 2017. The multifloat configuration includes 3 floats and the reactor base made of empty tanks to provide the required buoyancy.

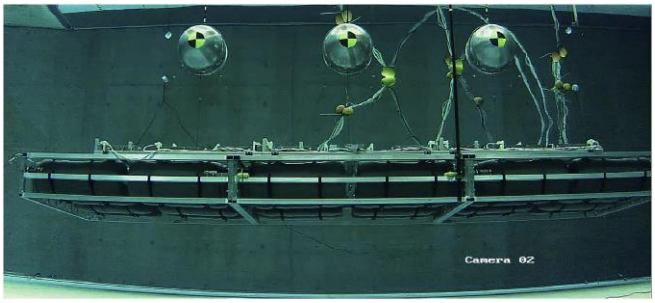

Fig. 1: 1:25 scale model of a multifloat configuration of the WaveSub device during experimental campaign in 2017 [20].

II. MATERIAL AND METHODS

A. Methods

The numerical model has been created in WEC-Sim [8] to solve the time-domain equation of motion for each hydrodynamic body in the 6 degrees of freedom. The response of the device is obtained solving the equations of motion of the WEC in 6 degrees of freedom [22] as shown in

$$(m + A_\infty)\vec{X}'' = -\int_0^t K(t-\tau)\vec{X}'(\tau)d\tau + \vec{F}_{ext} + \vec{F}_{vis} + \vec{F}_{res} + \vec{F}_{PTO} + \vec{F}_{mo} \quad (1)$$

where m is the mass matrix, A_∞ is the infinite frequency added mass matrix, $\vec{X}$ is the displacement and rotational vector of the body, K is the matrix of impulse response function, $\vec{F}_{ext}$, $\vec{F}_{vis}$, $\vec{F}_{res}$, $\vec{F}_{PTO}$ and $\vec{F}_{mo}$ are the vector of wave-excitation force, quadratic viscous drag force, net buoyancy restoring force, PTO force and the mooring force.

Frequency-domain hydrodynamic coefficients are used in WEC-Sim and these are generated in advance by using the open-source software, Nemoh [7], which is based on linear potential flow theory to calculate the frequency domain excitation, added mass, and radiation damping coefficients. Hydrodynamic interaction of all the hydrodynamic interaction bodies is also computed. It agrees well with commercial software such as Wamit [23], [24].

WEC-Sim code has been updated in this work to include the capability to simulate a frequency-directional distribution. This has been obtained mainly by adding the calculation of the wave distribution to the code and by modifying the calculation of the wave elevation and of the excitation force.

The wave elevation is described as:

$$\eta(x,y,t) = \sum_{i=1}^{N_f}\sum_{j=1}^{N_d} A_{ij}\cos\big(2\pi f_i t - k_i \cdot \big(x\cdot cos(\theta_j) + y\cdot sin(\theta_j)\big) + \Phi_{ij}\big) \quad (2)$$

where A_{ij}, f_i, k_i, θ_j, Φ_{ij} are respectively the amplitude, the frequency, the wave number, the direction and the phase for each incident directional wave evaluated for a specific point of the wave field (x,y) and a specific instant of time (t). N_d and N_f are the number of wave directions and frequencies (the example shown later has 7 and 952 respectively). A larger number of wave directions and wave frequencies will increase the accuracy of the wave elevation. Their number have been limited in this study because of computational time reasons. The amplitude spectrum is related with the frequency (S_i) and frequency-directional distribution (D_{ij}) for a discretized frequency step (Δf) and direction step ($\Delta\theta$) as [25]

$$A_{ij} = \sqrt{2S_i D_{ij}\Delta f_i \Delta\theta_j} \quad (3)$$

The sum of the directional components for each frequency is dependent on the frequency-directional amplitude spectrum. The frequency-directional distribution needs to fulfil the requirement

$$\sum_{j=1}^{N_d} D_{ij}\Delta\theta_j \cong 1 \quad (4)$$

for each frequency f_i.

The discretization of the directional distribution for a limited number of directions makes this integral less accurate. So, a correction factor has been applied to each frequency of the distribution in order to respect equation (4).

There are different frequency-directional distributions that have been modelled in the code generated for this work (See Fig. 2). These are the uniform, the Mitsuyasu, the Hasselman, the Donelan-Banner, and a more general user imported frequency-directional distribution option. The formulation of the distributions is expressed in the formulas (5-7).

The 'Uniform' distribution is uniform in the frequency-domain, but follows a distribution in direction. It is described as a cosine-fourth spreading function and it is expressed as [2]

$$D(\theta) = \begin{cases} \frac{8}{3\pi}\cos^4(\theta-\theta_m) & -\frac{\pi}{2}+\theta_m < \theta < \frac{\pi}{2}+\theta_m \\ 0 & otherwise \end{cases} \quad (5)$$

where θ_m is the main wave direction considered as 0 degrees.

The other distributions are instead dependent both on the wave frequency and direction. The Mitsuyasu and the Hasselman distributions are described both as

$$D(f,\theta) = G(s)\cos^{2s}\left(\frac{\theta-\theta_m(f)}{2}\right) = \frac{2^{2s-1}}{\pi}\frac{\Gamma^2(s+1)}{\Gamma(2s+1)}\cos^{2s}\left(\frac{\theta-\theta_m(f)}{2}\right) \quad (6)$$

where Γ is the gamma function and s is the spreading parameter dependent on the frequency. However, the spreading parameter is obtained in a different way

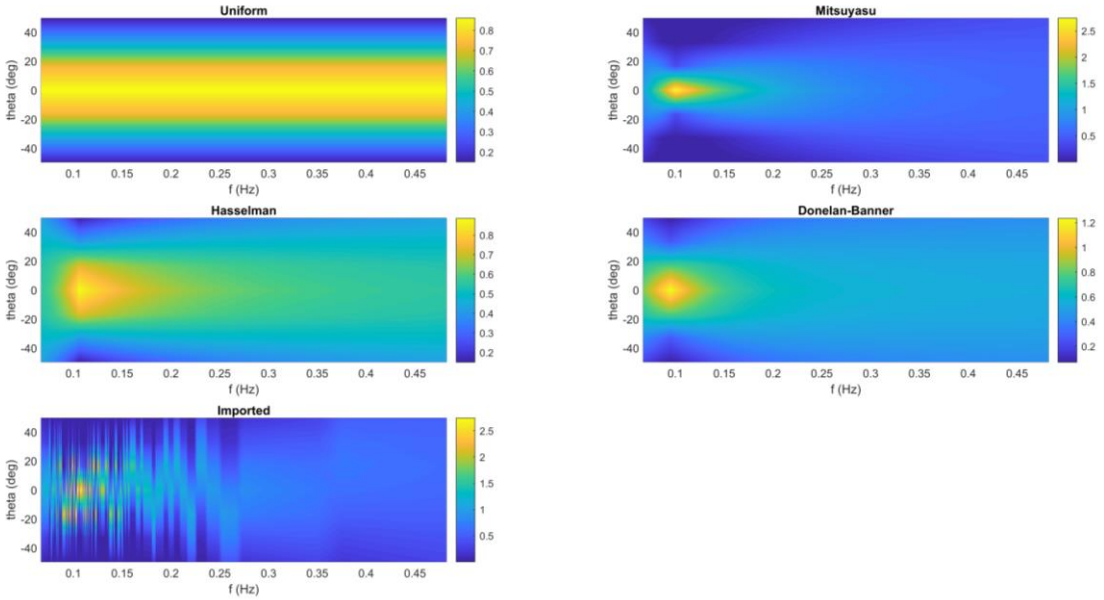

Fig. 2: Frequency-directional distributions compared in this work. These are the uniform, the Mitsuyasu, the Hasselman, the Donelan-Banner and a user imported option. An example for the user option is shown and it is the Mitsuyasu with a random mean wave direction obtained for each frequency range chosen.

between the Mitsuyasu and the Hasselman and it depends on their different location. Further details for the calculation of the spreading parameter are given in [13].
The Donelan-Banner frequency-directional distribution is given as

$$D(f,\theta) = 0.5\beta \operatorname{sech}^2 \beta \left(\theta - \theta_m(f)\right) \tag{7}$$

where β is a function of $\frac{f}{f_p}$ [13].
All of the above distributions are shown in Fig. 2. Finally, there is an option for a fully user specified distribution; this distribution can be arbitrary and could be used to replicate conditions in a wave tank for example. In the comparisons used in this paper, a random mean wave direction is chosen for each frequency step combined with the Mitsuyasu directional distribution, as shown in Fig. 2.

The excitation force is the only hydrodynamic load that depends on the wave direction and frequency-directional distribution chosen. So, this required change is implemented in the open source WEC-Sim software. The frequency-directional excitation coefficients ($\vec{F}_{ex\_ij}$) can be expressed as a complex number because both the amplitude and the phase are important for the time domain formulation of the excitation force ($F_{ex}(t)$). It is expressed as

$$\vec{F}_{ex\_\mathrm{ij}} = |F_{ex\_ij}| \cdot \exp\left(i\Phi_{ex_{ij}}\right) \tag{8}$$

where $|F_{ex\_ij}|$ is the amplitude and $\Phi_{ex_{ij}}$ is the phase of the excitation coefficient for each frequency and direction.
The extended time domain formulation of the excitation force ($F_{ex}(t)$) is expressed as

$$\begin{aligned} \vec{F}_{ex}(t) = \\ \sum_{\mathrm{i}=1}^{N_f}\sum_{\mathrm{j}=1}^{N_d} A_{ij} \cdot Re\left(\vec{F}_{ex_{\mathrm{ij}}} \cdot \exp\left(i2\pi f_i t + \Phi_{ij}\right)\right) = \\ \sum_{i=1}^{Nf}\sum_{j=1}^{N_d} A_{ij} \cdot \left(Re\left(\vec{F}_{ex\_\mathrm{ij}}\right) \cdot \cos\left(2\pi f_i t + \Phi_{ij}\right)\right. \\ \left. - Im\left(\vec{F}_{ex\_\mathrm{ij}}\right) \right. \\ \left. \cdot \sin\left(2\pi f_i t + \Phi_{ij}\right)\right) \end{aligned} \tag{9}$$

where $\vec{F}_{ex\_i}$ are the complex frequency excitation coefficients obtained from Nemoh. $F_{ex}(t)$ is dependent on the frequency-directional distribution because of the amplitude spectrum (A_{ij}) dependent on the distribution (See formula (3)). The discretization of the wave elevation (Eq. 2) for a certain number of wave frequencies and directions will have some impact also in the accuracy of the computation of the excitation force. A sensitivity analysis can probably clarify the impact of their number on the computation of the excitation load. Again, their number have been limited in this study because of computational time reasons.

It is well known that the energy yield of a WEC varies significantly with the stiffness and damping parameters of the system. To ensure that comparison between wave spreading descriptions is fair, the WEC should be optimal for that wave climate. Therefore,
an optimisation of the WEC to maximise the power produced for the frequency-directional distribution chosen is carried out using the optimiser described in [19], [26], [27]. The total power produced is obtained as

$$\mathrm{P} = \sum_{i=1}^{Nlines} \mathrm{c_{PTO}} \cdot \mathrm{v}_i^2 \tag{10}$$

where $Nlines$ are the number of PTO corner lines, $\mathrm{c_{PTO}}$ is the damping coefficient of the PTO and $\mathrm{v_i}$ is the corner PTO line speed. The PTO line speed is due to the spring-damping modelling of each corner PTO line. More specifically, there will be a pulley system on the reactor that will allow the physical modelling of the PTO.
The four corner PTO lines are simplified each as a linear spring-damper where the damping coefficient produce power. There is also a central PTO line that is used to give the required preload to the float and it is simplified as a linear spring.

The design parameters are the stiffness and damping of the PTO corner lines (See Fig. 3). The design space is based from MPS experience and a screening check while the design constraint has been obtained through a significant penalty function for the simulations outside the design range. The hydrodynamic coefficients obtained from Nemoh are also an input for the time-domain simulation of WEC-Sim that are the same ones

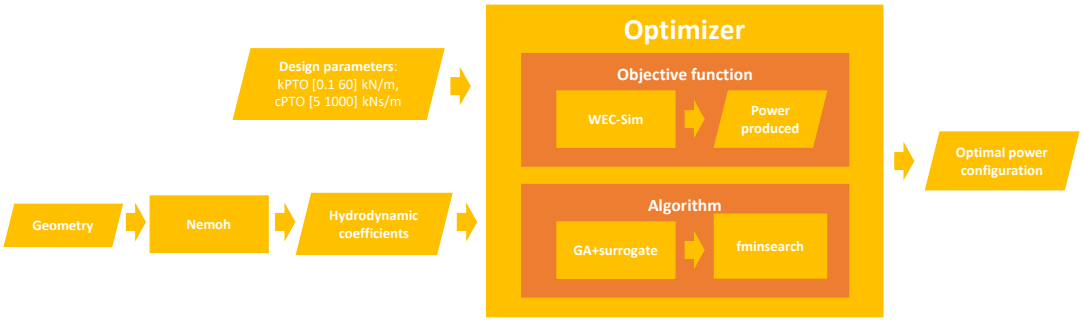

Fig. 3: Optimisation scheme.

used for the different directional distribution optimisation cases. The optimisation algorithm chosen combines three approaches to give a global free gradient method. An open-source genetic algorithm [28] has been upgraded as described in [19]. Secondly, the genetic algorithm is combined with the Kriging surrogate model [29]. The surrogate model is used to estimate some of the new individuals of the new generation of the genetic algorithm using an elitism factor. The MATLAB "fminsearch" function has been then added in the last part of the optimisation to allow the final convergence to the optimum. The optimisation considers the genetic algorithm with 5 generations and 20 individuals and an elitism factor of 50%. The "fminsearch" function is then used in the last 30 simulations.

Finally, the amplitude spectrum of the float and of the reactor has been obtained using the MATLAB function pwelch. In particular, the pwelch function is used to find the spectral density of the motion (M_i) and then the amplitude spectrum is calculated as

$$\mathrm{A}_i = \sqrt{2 \cdot \Delta f \cdot M_i} \tag{11}$$

B. Computational model set-up

A full-scale WaveSub device is simulated and the main geometry and mass parameters are given in Table 1 and Fig. 4.

Table 1: Geometry and mass properties of the float and of the reactor.

Geometry and mass parameters	
Float diameter (m)	12
Float depth (m)	-10.5
Float cylinder length (m)	4.75
Float mass (kg)	109'500
Float inertia moments I_{xx}, I_{yy}, I_{zz} (kg m^2)	$[4.047\ 2.997\ 4.047] \cdot 10^6$
Reactor size (m×m×m)	51.55×50×10.5
Reactor depth (m)	-33
Reactor mass (kg)	13'238'000
Reactor inertia moments I_{xx}, I_{yy}, I_{zz} (kg m^2)	$[2.880\ 3.053\ 5.690] \cdot 10^9$

The float has a capsule shape with a short cylinder in the middle and two hemispheres in the sides while the reactor has a cuboid shape. The body properties such as the mass and the inertia are simulated using the "Hydrodynamic Body" block from WEC-Sim library. PTO and moorings are modelled in the same way as a simple spring-damping term using the "Translational PTO Actuation Force" block from the WEC-Sim library. Lower and upper joints for each line are modelled as universal and gimbal joints respectively. In this way, if needed, torsional loads could be also obtained. The central PTO line is a simple spring (586 MN/m) while the stiffness-damping coefficients of the 4 corner PTO lines are optimised for each frequency-directional distribution case. The range of PTO stiffness considered in the optimisation is between 0.1-60 kN/m while the PTO damping is considered between 5-1000 kNs/m. The reactor is connected to the seabed with 4 taut mooring lines and they are modelled as a simple spring-damping term with a mooring stiffness of 3.19 MN/m and a mooring damping of 1 kNs/m. Wave direction has the same direction of x axis.

A quadratic viscous drag term is used in the model and it is expressed as

$$\vec{\mathrm{D}} = \frac{1}{2} C_d \rho_w A \vec{v} |\vec{v}| \tag{12}$$

where C_d is the drag coefficient, ρ_w is the water density, A is the characteristic area and $\vec{v}$ is the body velocity.

A drag coefficient of 0.7 has been chosen based on benchmarking of a WaveSub device with experimental data in [20].

Hydrodynamic coefficients simulated in Nemoh are obtained for a water depth of 100m and for wave frequencies and directions described in Table 2. A mesh sensitivity of the float and the reactor hydrodynamic coefficients for the main direction is given in Appendix A. The frequency-domain spectrum chosen is the Pierson-Moskowitz with a significant height of 1m and an energy period of 10s and it considers 952 frequencies.

The wave directions and step are consistent with earlier work [17]. The wave directions are chosen between the main direction and two times the wave direction spread of the Berth A buoy of the Belmullet site (σ = 28.95 deg) with a total directional range between -57.9 deg and 57.9 deg. This gives a probability of 95.45% of the real incoming directional wave for a uniform Gaussian distribution as described in [17] and shown in Fig. 5. This is considered just as an example for the comparison and there is no aim to represent a realistic location. Seven wave directions are sufficiently accurate due to the increasing computational time for a larger number of directions. The number of wave directions and uniformly distributed directional steps are consistent with Equations 3 and 4. The directional step and the main directions are chosen respectively as

$$\Delta\theta = \frac{2}{7}\sigma \tag{13}$$

and

$$\theta_j = n \cdot \Delta\theta \tag{13}$$

where n is an integer number chosen between -3 and 3, the resulting values are shown in Table 2.

Table 2: Wave directions chosen to obtain the hydrodynamic coefficients.

Wave frequencies						
Min (rad/s)		**Max (rad/s)**		**Number**		
0.02		5		952		
Wave directions (Deg)						
-49.63	-33.09	-16.54	0.00	16.54	33.09	49.63

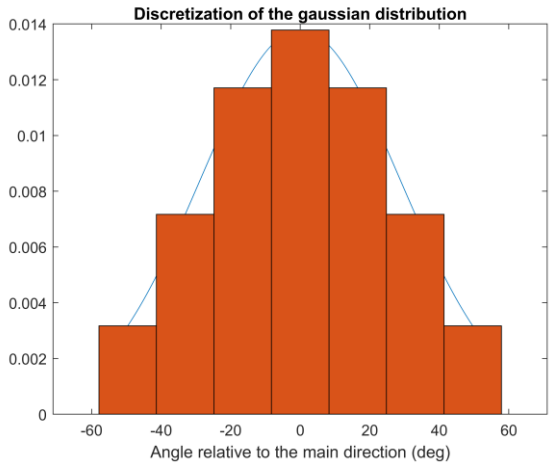

Fig. 5: The discretization of the directional distribution for the uniform distribution.

III. PREVIOUS WORK

The current work is based on the previous paper presented at the EWTEC conference in 2019 [17]. In this

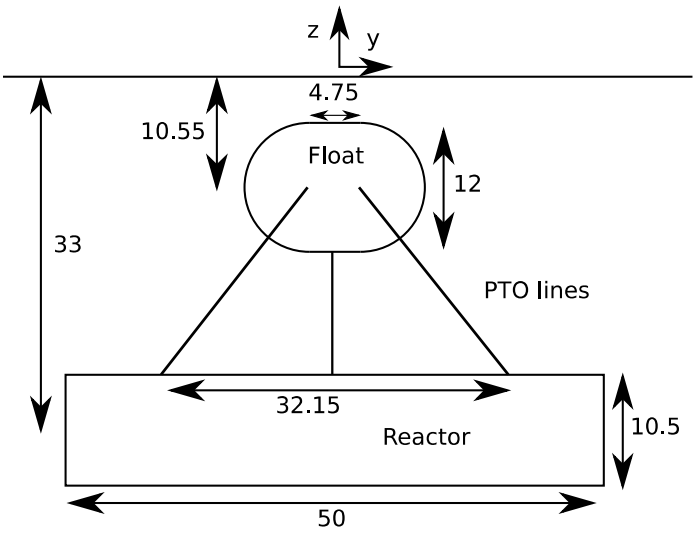

(a)

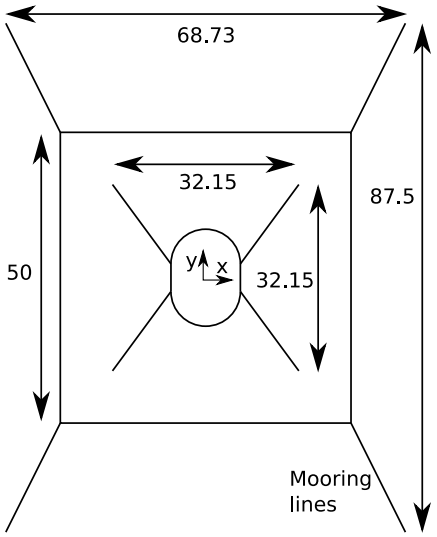

(b)

Fig. 4: Schematic of the WaveSub configuration.

previous work a Gaussian directional distribution independent of the frequency was implemented in the numerical model. A discretized number of wave directions between the main direction and 2 times the wave direction spread of the Belmullet site were used to give a probability of 95.45% of the real incoming directional wave. The excitation force and the wave fields namely as the incident, diffracted, radiated and perturbed wave fields were also formulated to understand the influence of the directional distribution compared to a single direction case. The WaveSub device considered in this work is found to move mainly in surge, heave and pitch for a single wave direction while it starts to move in the other degrees of freedom for multi-directional waves. Both [17] and the current work use the same device model and design parameters. The numerical inputs are very similar with only the significant wave height updated to 1m to respect better the linear theory used in the model and the drag coefficient updated to 0.7 following the experimental work presented in [20]. The same mesh is used in both studies and the mesh convergence study is shown in the Appendix A.

One of the main differences compared to the current paper is that the earlier study was limited to a uniform frequency distribution only referred to the Belmullet site. Therefore, in the extension presented here, different directional distributions relative to different locations have been discretized into a number of directions and frequencies including also the optimisation of the PTO parameters for each of them.

IV. RESULTS

Sensitive results for two distributions (non directional and uniform) and three different maximum timestep have been provided in Table 3. The simulation solver is ode45 that uses an adaptive timestep in which the minimum timestep is automatically computed and the maximum one is defined by the user. Results are then interpolated for a constant timestep equal to the maximum one. The sensitivity of the timestep shows that the largest one considered (0.1s) is enough accurate for optimisation purposes in which a computational efficient simulation is required.

Table 3: Sensitivity of normalized mean power (-) influenced by the timestep for kPTO of 30 kN/m and cPTO of 500 KNs/m for the non-directional and uniform distributions.

	d*t*=0.02s	**d*t*=0.06s**	**d*t*=0.1s**
No directional	0.981	0.998	1.000
Uniform	0.974	0.994	1.000

Each model of a frequency-directional distribution will have a different optimal PTO stiffness and damping. So, an optimisation for each case has been completed as discussed in section 2.1 and the results are shown in Fig. 6. Optimal PTO parameters of each distribution are compared to have a more fair comparison of the tuned optimal power. The results of the optimisation show that the optimal PTO parameters are anyway quite similar between the distributions as shown in Table 4. Generally, the optimal PTO stiffness is in the low range while the optimal damping is in the middle range. Fig. 6 demonstrates the convergence to the optimal PTO stiffness is slower than to the optimal PTO damping. In fact, there is a larger number of simulation points (red points in Fig. 6) next to the optimal PTO damping than to the optimal PTO stiffness. The power produced is also more sensitive to the PTO damping as evident from the colour variation of Fig. 6 and so, this last parameter is easier to optimise and converges faster. The optimal power produced from the frequency-directional distribution cases is lower than the single direction case as expected and as shown in Fig. 7. In fact, the power produced from the distribution cases is smaller because of the reduced effect of the excitation force on the dynamics of the WEC that is spread to all degrees of freedom. In fact, it is expected that some of the excitation components will cancel each other out because of the different excitation directional components. Fig. 7 shows that the power produced is decreased between 10-20% for the distribution cases. In particular, the Mitsuyasu distribution has the least reduction in power capture compared to the other cases while the Hasselman distribution has the highest. Finally, the Donelan-Banner, the imported and the uniform distribution cases have a similar optimal power value.

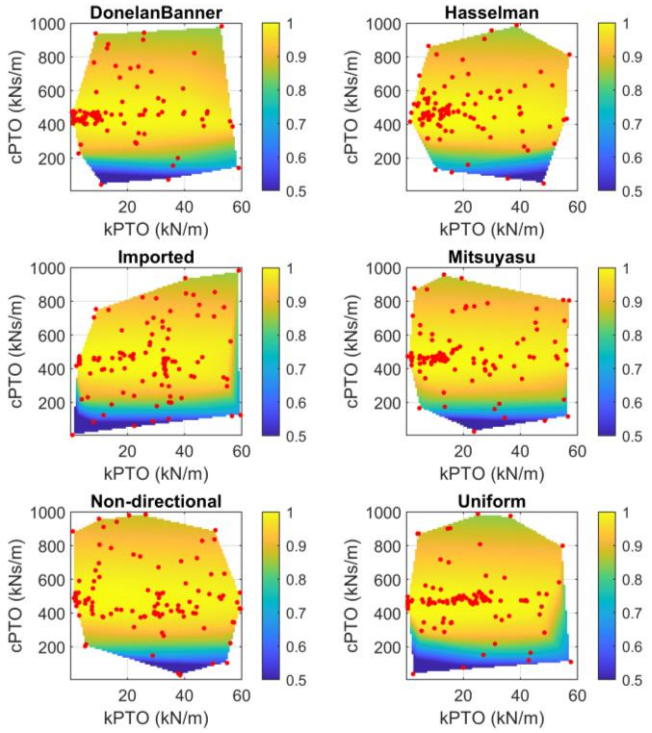

Fig. 6: Visualisation of the optimisation search space, with the colour bar showing the power produced, normalized to the maximum power produced in the non-directional case. Red dots represent the simulation results. Each panel shows a different distribution.

Table 4: The first 2 columns show the optimal PTO stiffness and damping for the different optimisation cases.

	kPTO (kN/m)	cPTO (kNs/m)
Non-directional	1.81	492.81
Uniform	0.55	454.28
Mitsuyasu	1.84	469.26
Hasselman	7.81	454.15
Donelan-Banner	1.13	454.14
Imported	3.12	444.57

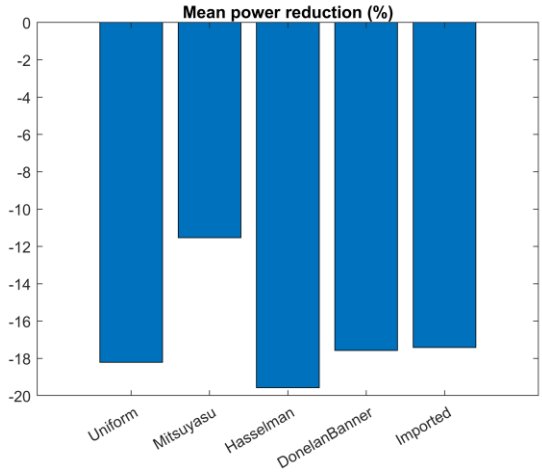

Fig. 7: Reduction of the mean power between the frequency-directional distribution cases and the non-directional case.

Fig. 8 shows a comparison of the amplitude spectrum of the float and of the reactor for all their degrees of freedom between the optimisation cases while Table 5 shows a comparison between their root mean square (rms) value. These results were obtained using the wec-sim option "Traditional" for the discretisation of the wave frequencies, as a better representation of the spectrum was found with this option instead of the "Equal energy" option used for the other results, while the statistical properties in terms for example of mean power and rms motion are similar between the two options (generally 2-3% difference). The difference between the two options is that the first imports the wave frequencies with same frequency step while the latter imports wave frequencies with a larger number next to the peak frequency. The hydrodynamic coefficients of Nemoh are then interpolated for the simulated frequencies. Fig. 8 gives a better understanding of the frequency response of the different hydrodynamic bodies. For the non-directional case, the motion for both the float and the reactor are mainly in surge, heave and pitch. However, the frequency-directional distribution introduces motion also in the other degrees of freedom such as sway, roll, and yaw (See Fig. 8). The spectrum of the float has one main peak around 0.12-0.14 Hz for the different degrees of freedom. This peak is influenced by the hydrodynamic excitation coefficients of the float, which have a peak around this frequency. The motion amplitude spectrum of the reactor is shifted towards lower frequencies and has a peak around 0.08 Hz, as its dynamic response is in a lower frequency range compared to the float due to its larger size. However, the pitch spectrum of the reactor has a higher frequency peak (0.13-0.14 Hz), which could be due to the fact that the pitch excitation coefficients of the reactor have a higher frequency response than the surge and heave excitation coefficients (see Fig. A.1). Table 5 helps to understand more clearly the significance of the motion for each degree of freedom and optimisation case. A large rms value is correlated with a larger motion. The surge and heave rms of both the float and reactor are, generally, the most significant motion. Surge and heave rms of the float are quite similar especially for the non-directional case. The reactor, instead, presents a larger difference between them with the heave rms larger than surge. Sway rms is negligible for the non-directional case while it appears more significant for the distribution cases around 2 to 7 times smaller compared to surge and heave rms for both float and reactor. Finally, pitch is the main rotational motion, especially for the non-directional case. Pitch value is similar between all the optimisation cases and for both float and reactor. Roll and yaw of float and reactor are negligible for the non-directional case. They become more significant for the float and the directional cases around 2 to 4 times smaller compared to pitch. The reactor yaw is quite negligible for the distribution cases as well but the reactor roll is more significant for the directional cases around 3 to 11 times smaller compared to pitch.

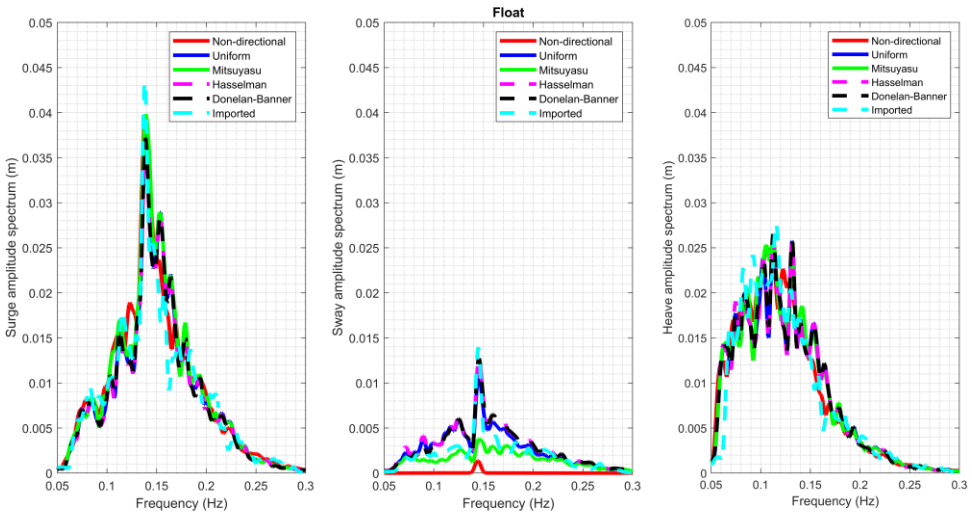
Float
Non-directional
Uniform
Mitsuyasu
Hasselman
Donelan-Banner
Imported
Surge amplitude spectrum (m)
Sway amplitude spectrum (m)
Heave amplitude spectrum (m)
Frequency (Hz)

(a)

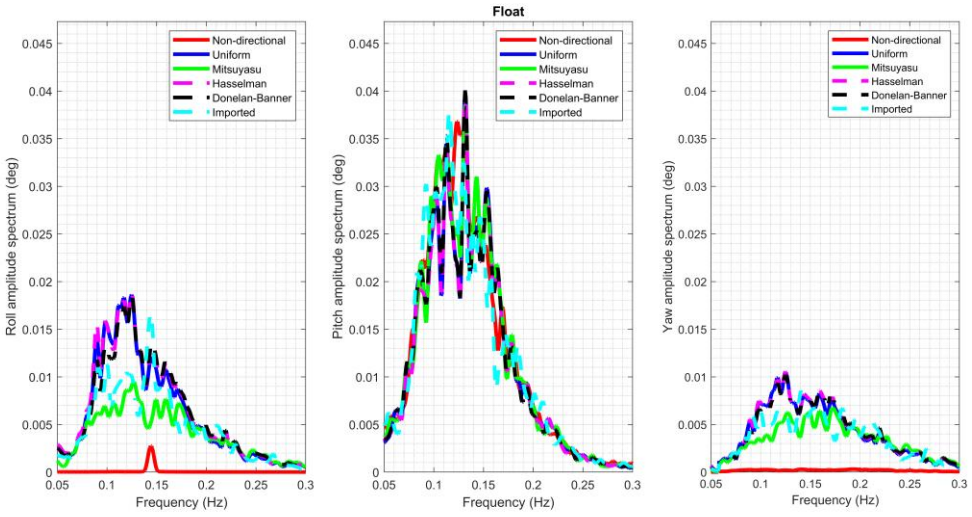
Float
Non-directional
Uniform
Mitsuyasu
Hasselman
Donelan-Banner
Imported
Roll amplitude spectrum (deg)
Pitch amplitude spectrum (deg)
Yaw amplitude spectrum (deg)
Frequency (Hz)

(b)

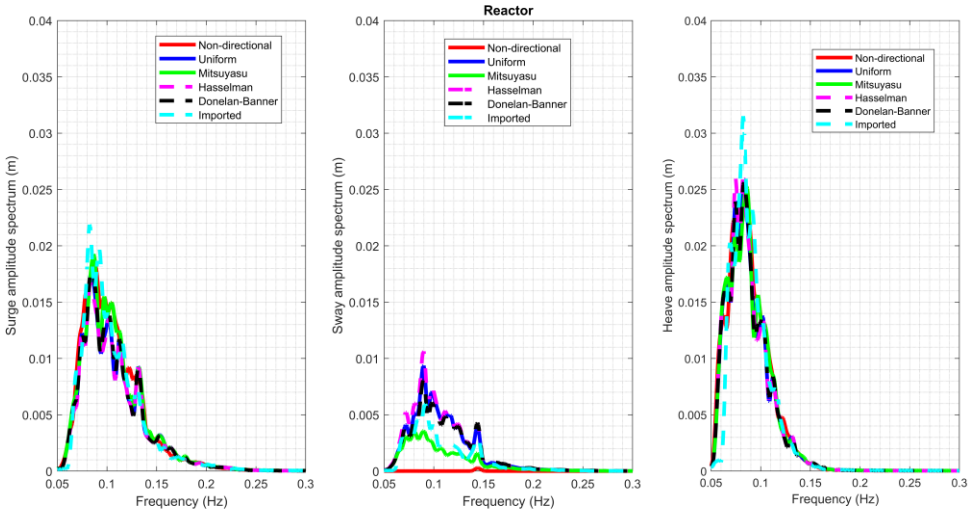

(c)

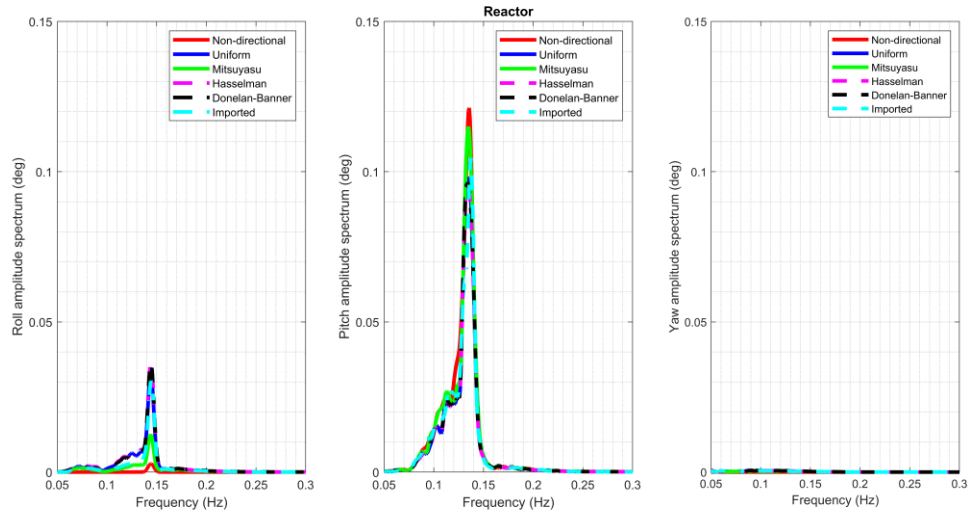

(d)

Fig. 8: Amplitude spectrum for all 6 degrees of freedom of the float (a,b) and of the reactor (c,d) for the different optimization cases.

Table 5: Float and the reactor motion timeseries rms for the different optimization cases and for Hs=1m and Te=10s.

Sea state H_s=1m and T_e=10s							
Root mean square		Surge (m)	Sway (m)	Heave (m)	Roll (deg)	Pitch (deg)	Yaw (deg)
	Non-directional	0.1526	0.0028	0.1467	0.0117	0.2115	0.0025
	Uniform	0.1480	0.0427	0.1433	0.1019	0.1961	0.0644
	Mitsuyasu	0.1581	0.0224	0.1449	0.0604	0.2056	0.0469
	Hasselman	0.1440	0.0475	0.1428	0.1060	0.1925	0.0665
	Donelan-Banner	0.1452	0.0466	0.1434	0.1011	0.1969	0.0642
Float	**Imported**	0.1458	0.0353	0.1404	0.0772	0.1978	0.0537
	Non-directional	0.0866	0.0005	0.1052	0.0053	0.2846	0.0003
	Uniform	0.0755	0.0350	0.1026	0.0639	0.2517	0.0143
	Mitsuyasu	0.0811	0.0170	0.1009	0.0256	0.2848	0.0065
	Hasselman	0.0741	0.0389	0.1043	0.0706	0.2447	0.0162
	Donelan-Banner	0.0767	0.0325	0.1028	0.0703	0.2478	0.0109
Reactor	**Imported**	0.0833	0.0228	0.1036	0.0563	0.2399	0.0100

A. Wave field

The total wavefield can be also obtained from the hydrodynamic free surface frequency-domain coefficients and time-domain results as described in [17]. The time-domain results of the body velocity and wave elevation have been converted to the frequency-domain using the Fourier transform. Good matching with the hydrodynamic frequencies, that is necessary for the wavefield calculation, is obtained by choosing a simulation time of 1202s (without ramp time) and a time step of 0.02s. More specifically, the reciprocity relationship between the hydrodynamic frequency step (Δf) and the WEC-Sim simulation timestep (Δt) is required to have a higher accuracy of the wave field as explained in [17]. The reciprocity relationship is expressed as

$$\Delta f \cdot \Delta t = \frac{1}{L} \tag{15}$$

where L is the length of the simulation signal.
The simulation time is also enough long to represent the statistical results of the irregular sea state [30]. The number of field points used is 50 points in x and y while the field area covers 100m in each dimension. So, each point covers an area of 4m².

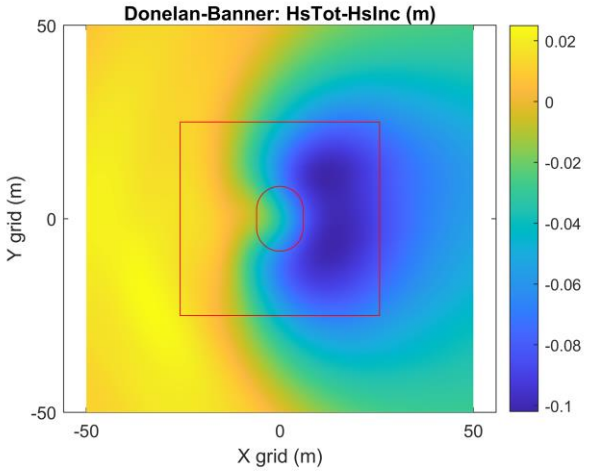

(a)

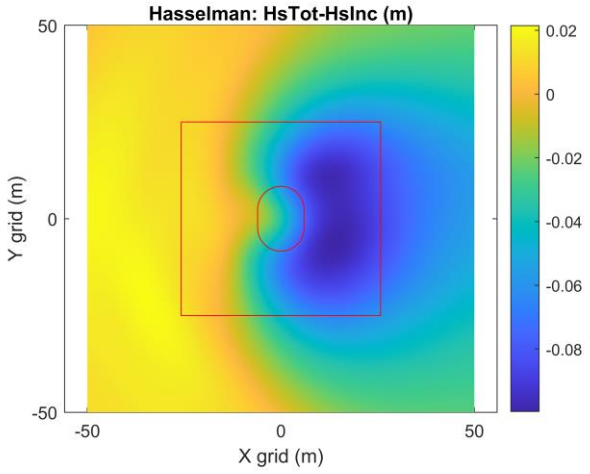

(b)

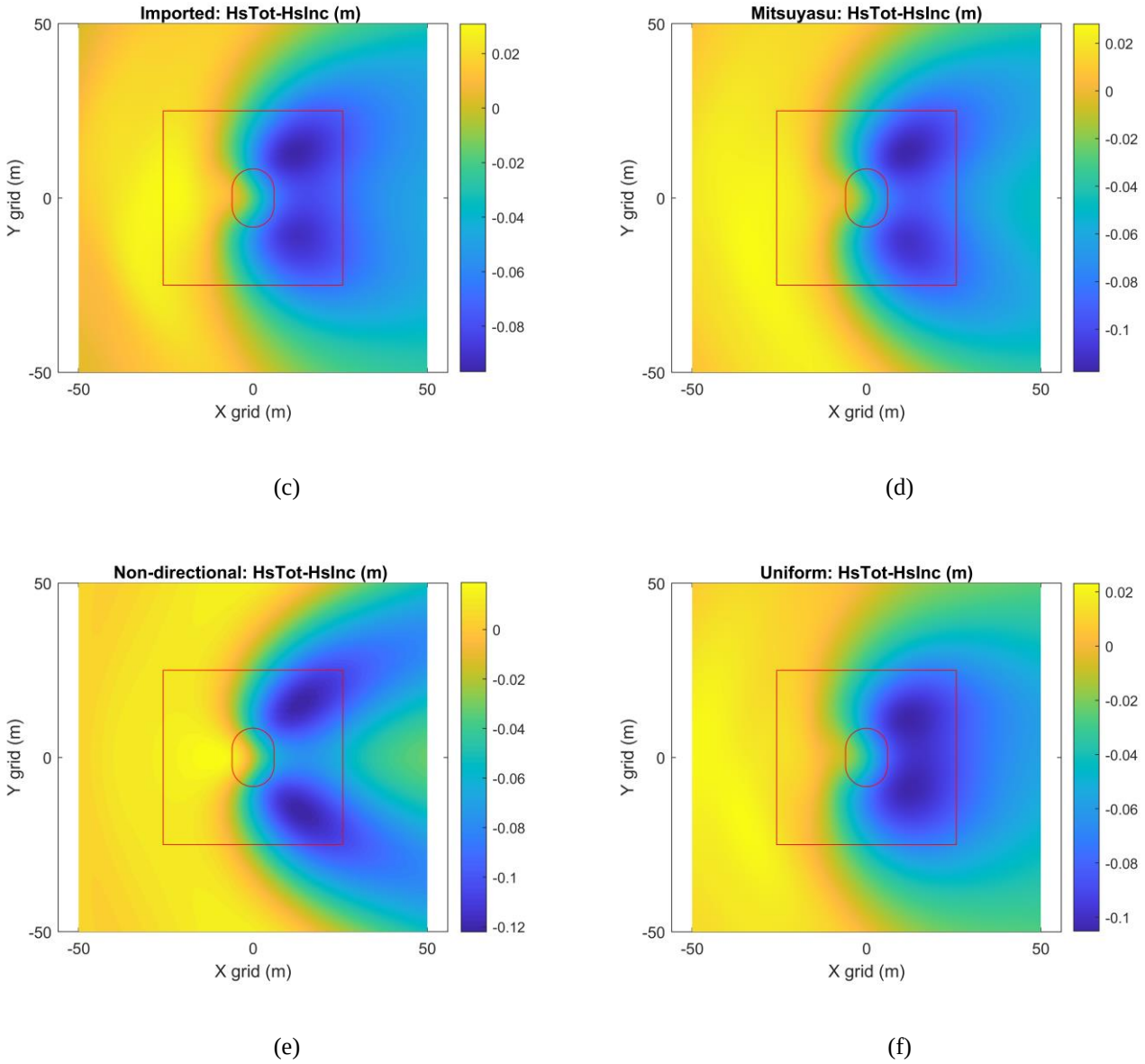

(c) (d)

(e) (f)

Fig. 9: Difference between the total and the incident significant height wavefields for the different distributions. Front and back of the device are left and right respectively.

Fig. 9 shows a comparison of the difference in the significant wave height between the distribution cases. The total significant height refers to the significant height generated by the total perturbed field that is the sum of the incident, diffracted and radiated wave fields. There is an increase for both above the float position at rest and behind. More specifically, the float generates an increase of the total significant height that follows a parabolic shape centered on the float due to the interaction between the diffraction and radiation fields. The directional distribution cases show a more uniform significant height compared to the non-directional case that is especially evident in the back of the device and looking at the lower value of the colour scale. This is probably due to the averaging effect of the wave direction that reduces the variation of the significant height. In fact, the non-directional distribution shows a second peak in the back of the device while the other distributions such as the Donelan-Banner, Hasselman, and uniform distributions have a unique drop off valley. The Mitsuyasu and the imported distributions (recall that this last is arbitrarily chosen as the Mitsuyasu with as a random mean wave direction) have also a noticeable second peak but still less evident than the non-directional distribution as expected.

V. DISCUSSION

The evaluation of the performance of the WaveSub device for different directional distributions has been limited to a single sea state. This is an important limitation of this study where generally multiple sea states should be considered. A site location will be

characterized, generally, with an occurrence matrix in which each sea state can be described by the frequency spectrum and a directional distribution. However, the main aim of this study has been to compare the performance of the WEC for directional distributions with a similar wave spectrum and not to compare different locations. Furthermore, we think that this work is also significant for a preliminary performance analysis because the same approach presented here could be used to simulate an arbitrary chosen frequency-directional distribution to estimate the performance of a WEC.

The results of this study have limitations related to the implementation of the frequency-directional distribution in the time domain code. In-fact, the directional distribution accuracy is limited by the number of wave directions. A finer discretization of the wave direction range will increase the accuracy of equation 4 in which the sum of the directional components of the directional distribution for each frequency must be equal to 1. This work has used a scaling factor to solve this error generated by the discretization. However, this will introduce also some distortion of the original theoretical directional distribution with a consequent loss of accuracy. At the same time equation 9 shows that the computation of the excitation force is also influenced by the number of directions and the directional distribution. So, it is recommended that the number of wave directions chosen is the largest as possible to reduce these effects. This work has limited the number of directions to seven because the software used for the computation of the hydrodynamic coefficients is computationally expensive especially for the computation of the wave fields.

The numerical model used in this work is a time domain model that accounts of some of the nonlinear loads such as the quadratic drag. Other possible nonlinear hydrodynamic loads that could be related to the hydrostatics and the Froude-Krylov loads are not considered. In fact, they are supposed to have a small influence on the results because the device is totally submerged and also because a small sea state has been accounted. The nonlinear computation of the Froude-Krylov has been investigated in [31], [32] while a review of nonlinear approaches to compute the hydrodynamics loads can be found in [33], [34]. A larger wave will need to account nonlinearities from the wave steepness which could potentially lead to sub and superharmonics effects. In this case a weakly or a fully nonlinear model will be necessary to account a more accurate computation of the interaction between the floating body and the waves. The model has been simplified regarding the PTO and the mooring. They have been considered both as a simple spring-damping term but they should be probably more realistically represented for example as a hydraulic PTO or a lumped mass system respectively.

The optimal power results shown in Fig. 7 make sense with the directional distribution simulated. In fact, the Mitsuyasu distribution is the most similar to the non-directional distribution with a narrowest distribution around the main direction and so, a less negative directional effect on the power performance. On the other side, the Hasselman distribution is the most spread one with a larger negative drop in the power produced. The effect of the random wave direction applied to the last user specified distribution has also a negative impact on the power produced. The power produced is reduced for this case compared to the Mitsuyasu distribution with a single main direction. The comparison of the wave fields shown in Fig. 9 agree well also with the discussion of Fig. 7. Narrower distributions such as the Mitsuyasu have less uniform distributions compared, for example, to the Hasselman.

The results have shown also as expected that the main motion for the non-directional case is in surge, heave, and pitch because the device is symmetric compared to the wave direction. However, the frequency-directional distribution cases introduce a motion in the other degrees of freedom. The amplitude spectra have shown a different peak between the float and the reactor due to their different hydrodynamic resonance. The resonance of the reactor is expected to be for a lower frequency because of its larger size while the one of the float for a larger frequency.

VI. Conclusion

The effect of the frequency-directional spreading of waves on the performance of the WaveSub device has been investigated in this work. The time domain numerical model considers hydrodynamic loads calculated from a linear potential flow theory. A non-directional case has been compared to five frequency-directional spreading cases available from the literature. The five frequency-directional spreading approximations considered are the uniform cosine fourth, Mitsuyasu, Hasselman, Donelan-Banner, and a more general imported distribution with a random mean wave direction dependent on the frequency. An optimisation of stiffness and damping to maximise the power produced has been carried on for each case because of the possible different optimal settings. However, it was demonstrated that optimal PTO stiffness and damping are in a similar range for all cases. Results show that the power produced decreases by 10-20%. The Hasselman distribution has shown the largest impact on the performance of the WEC while the Mitsuyasu is the most similar to the non-directional case. The motion of the WEC is mainly in surge, heave, and pitch for the non-directional case while small amounts of sway, roll, and yaw appear for the spreading cases. Finally, the total wavefield generated by the WEC for the distribution case is more uniform than the non-directional case.

The methodology presented in this work for modelling the effect of frequency-directional spreading could be really effective compared to a CFD approach due to the fact that the computational time required is expected to

be significantly lower [9], [10]. However, there are some possible drawbacks related to the accuracy of the results given from the model because for example due to the discretization for the number of wave directions. In the future, a sensitivity study will help to clarify this issue. A future possible benchmarking with experimental results will help to clarify the validity of this model to represent multi-directional waves. Finally, the comparison between the non-directional case and the frequency-directional cases has been given for a specific sea state while it could be extended in a further investigation to include more sea states.

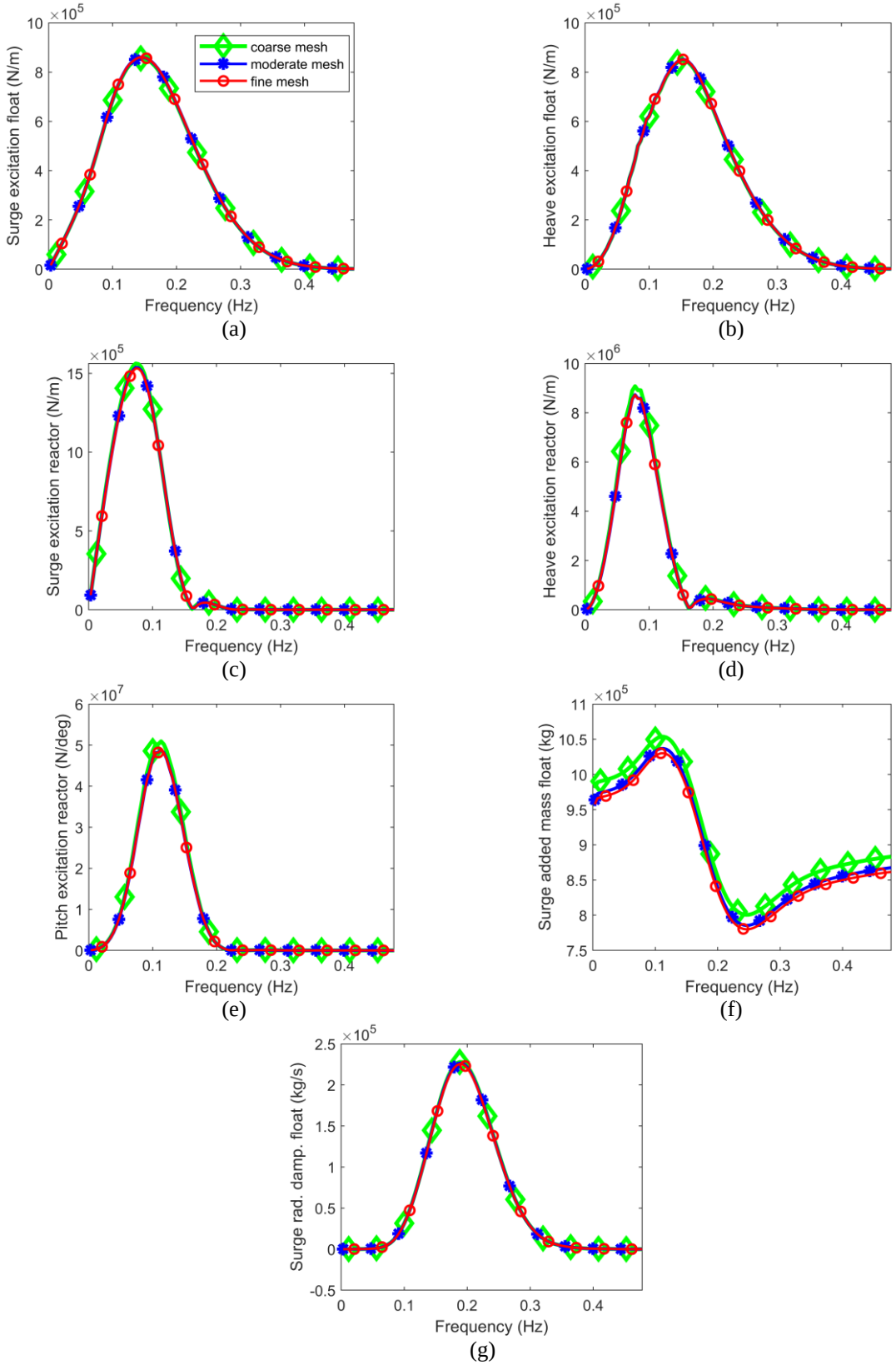

Fig. A.1: Surge, heave excitation coefficients of float (a,b), surge, heave and pitch of reactor (c,d, e), surge added mass coefficient and radiation damping of float (e,f).

APPENDIX A: MESH CONVERGENCE

A mesh convergence study has been undertaken to check the hydrodynamic results. This check has been limited to the main direction because it is the most important one that is influencing the results. Hydrodynamic coefficients are obtained for 952 wave frequencies between 0.02 and 5 rad/s.

Three different mesh of the float and the reactor are made using Salome-Meca [35]. The Netgen 2D hypothesis has been used to generate triangle panels with a similar minimum and maximum size of each panel element. These are a coarse mesh (201 panels for the float and 200 for the reactor), a moderate mesh (547 panels for the float and 877 for the reactor), and a fine mesh that is the one used in the time-domain model (868 panels for the float and 1501 for the reactor).

Fig. A.1 shows the results of the convergence for some of the hydrodynamic coefficients. Excitation coefficients are

expected to be significant only in surge, heave, and pitch because the device is symmetric compared to the wave direction. Fig. A.1a-b-c-d show the surge and heave excitation of the float and reactor. The frequency peak of the float is around 0.15 Hz while the peak of the reactor is moved to a lower frequency because of the larger size of the reactor.

Surge added mass and radiation damping of the float are also shown in Fig. A.1 e-f and they have been chosen just as an example. A very good convergence is possible to notice from all these plots.

REFERENCES

[1] Marine Power Systems Ltd, "WaveSub: The Future of energy," 2020. http://marinepowersystems.co.uk/.

[2] E. H. Song, "Directional Spreading Effect on a Wave Energy Converter," 2016.

[3] H. Mitsuyasu *et al.*, "Observations of the directional spectrum of ocean WavesUsing a cloverleaf buoy," in *Journal of Physical Oceanography*, 1975, vol. 5, no. 4, pp. 750–760, doi: 10.1175/1520-0485(1975)005<0750:ootdso>2.0.co;2.

[4] D. E. Hasselmann, M. Dunckel, and J. A. Ewing, "Directional wave spectra observed during JONSWAP 1973," in *Journal of physical oceanography*, 1980, vol. 10, no. 8, pp. 1264–1280, doi: 10.1175/1520-0485(1980)010<1264:dwsodj>2.0.co;2.

[5] M. A. Donelan, J. Hamilton, and W. Hui, "Directional spectra of wind-generated ocean waves," in *Philosophical Transactions of the Royal Society of London. Series A, Mathematical and Physical Sciences*, 1985, vol. 315, no. 1534, pp. 509–562, doi: 10.1098/rsta.1985.0054.

[6] M. L. Banner, "Equilibrium spectra of wind waves," in *Journal of Physical Oceanography*, 1990, vol. 20, no. 7, pp. 966–984, doi: 10.1175/1520-0485(1990)020<0966:esoww>2.0.co;2.

[7] A. Babarit and G. Delhommeau, "Theoretical and numerical aspects of the open source BEM solver NEMOH," 2015.

[8] K. Ruehl, Y.-H. Yu, J. Van Rij, and N. Tom, "WEC-Sim," 2020. https://wec-sim.github.io/WEC-Sim/ (accessed Mar. 30, 2020).

[9] M. Folley, *Numerical modelling of wave energy converters: state-of-the-art techniques for single devices and arrays*. Academic Press, 2016.

[10] E. J. Ransley *et al.*, "Focused wave interactions with floating structures: A blind comparative study," *Proc. Inst. Civ. Eng. Comput. Mech.*, vol. 174, no. 1, pp. 46–61, 2021.

[11] S. Michele, E. Renzi, C. Perez-Collazo, D. Greaves, and G. Iglesias, "Power extraction in regular and random waves from an OWC in hybrid wind-wave energy systems," *Ocean Eng.*, vol. 191, p. 106519, 2019.

[12] S. Michele, F. Buriani, E. Renzi, M. van Rooij, B. Jayawardhana, and A. I. Vakis, "Wave energy extraction by flexible floaters," *Energies*, vol. 13, no. 23, p. 6167, 2020.

[13] I. R. Young, *Wind generated ocean waves*. Elsevier, 1999.

[14] T. A. A. Adcock and P. H. Taylor, "Estimating ocean wave directional spreading from an Eulerian surface elevation time history," in *Proceedings of the Royal Society A: Mathematical, Physical and Engineering Sciences*, 2009, vol. 465, no. 2111, pp. 3361–3381, doi: 10.1098/rspa.2009.0031.

[15] A. Pecher, J. P. Kofoed, J. Espedal, S. Hagberg, and others, "Results of an experimental study of the Langlee wave energy converter," 2010.

[16] J.-C. Gilloteaux and J. Ringwood, "Influences of wave directionality on a generic point absorber.," 2009.

[17] E. Faraggiana, I. Masters, J. Chapman, G. Foster, and G. Stockman, "Multi-directional waves and time domain perturbed field visualization of the WaveSub device," 2019.

[18] Y.-H. Yu *et al.*, "WEC-Sim release," 2021. https://wec-sim.github.io/WEC-Sim/man/release_notes.html.

[19] E. Faraggiana, J. C. Chapman, A. J. Williams, and I. Masters, "Genetic based optimisation of the design parameters for an array-on-device orbital motion wave energy converter," *Ocean Eng.*, vol. 218, p. 108251, 2020, doi: 10.1016/j.oceaneng.2020.108251.

[20] E. Faraggiana *et al.*, "Computational modelling and experimental tank testing of the multi float WaveSub under regular wave forcing," *Renew. Energy*, vol. 152, pp. 892–909, 2020, doi: 10.1016/j.renene.2019.12.146.

[21] E. Faraggiana, I. Masters, and J. Chapman,

"Design of an optimization scheme for the wavesub array," 2018.

[22] A. Babarit, J. Hals, M. J. Muliawan, A. Kurniawan, T. Moan, and J. Krokstad, "Numerical benchmarking study of a selection of wave energy converters," in *Renewable energy*, 2012, vol. 41, pp. 44–63, doi: 10.1016/j.renene.2011.10.002.

[23] M. Penalba, T. Kelly, and J. Ringwood, "Using NEMOH for modelling wave energy converters: A comparative study with WAMIT," 2017.

[24] G. Parisella and T. Gourlay, "Comparison of open-source code nemoh with wamit for cargo ship motions in shallow water," *Cent. Mar. Sci. Technol. Curtin Univ. Tech. Rep*, vol. 23, 2016.

[25] A. F. O. Falcão, "Modelling of wave energy conversion," *Inst. Super. Técnico, Univ. Técnica Lisboa*, 2014.

[26] E. Faraggiana, J. C. Chapman, A. J. Williams, C. Whitlam, and I. Masters, "Investigation of new layout design concepts of an array-on-device WaveSub device," *Renew. Energy*, 2022.

[27] E. Faraggiana, M. Sirigu, A. Ghigo, G. Bracco, and G. Mattiazzo, "An efficient optimisation tool for floating offshore wind support structures," *Energy Reports*, vol. 8, pp. 9104–9118, 2022.

[28] X. Blasco, "Genetic algorithm," 2019. https://uk.mathworks.com/matlabcentral/fileexchange/39021-basic-geneticalgorithm.

[29] I. Couckuyt, T. Dhaene, and P. Demeester, "ooDACE toolbox: a flexible object-oriented Kriging implementation," *J. Mach. Learn. Res.*, vol. 15, no. 1, pp. 3183–3186, 2014.

[30] L. H. Holthuijsen, *Waves in oceanic and coastal waters*. Cambridge university press, 2010.

[31] G. Giorgi and J. V Ringwood, "Nonlinear Froude-Krylov and viscous drag representations for wave energy converters in the computation/fidelity continuum," *Ocean Eng.*, vol. 141, pp. 164–175, 2017.

[32] G. Giorgi, S. Sirigu, M. Bonfanti, G. Bracco, and G. Mattiazzo, "Fast nonlinear Froude--Krylov force calculation for prismatic floating platforms: a wave energy conversion application case," *J. Ocean Eng. Mar. Energy*, vol. 7, no. 4, pp. 439–457, 2021.

[33] M. Penalba Retes, G. Giorgi, and J. Ringwood, "A review of non-linear approaches for wave energy converter modelling," 2015.

[34] H. A. Wolgamot and C. J. Fitzgerald, "Nonlinear hydrodynamic and real fluid effects on wave energy converters," *Proc. Inst. Mech. Eng. Part A J. Power Energy*, vol. 229, no. 7, pp. 772–794, 2015.

[35] Code Aster, "Salome-Meca," 2019. http://www.code-aster.org/spip.php?article303.